Chapter 5
Low Cycle Fatigue Behavior at RT

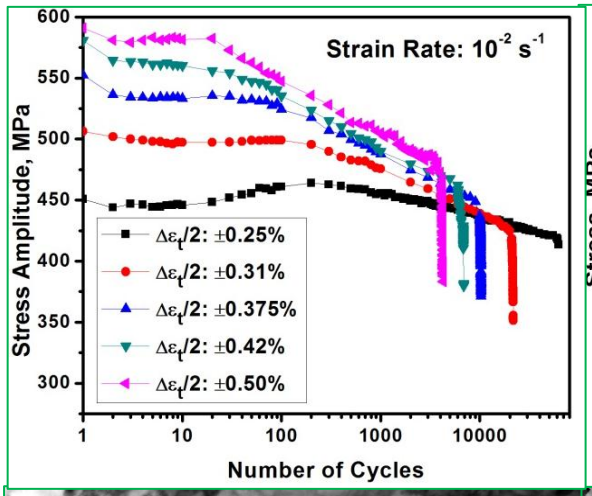

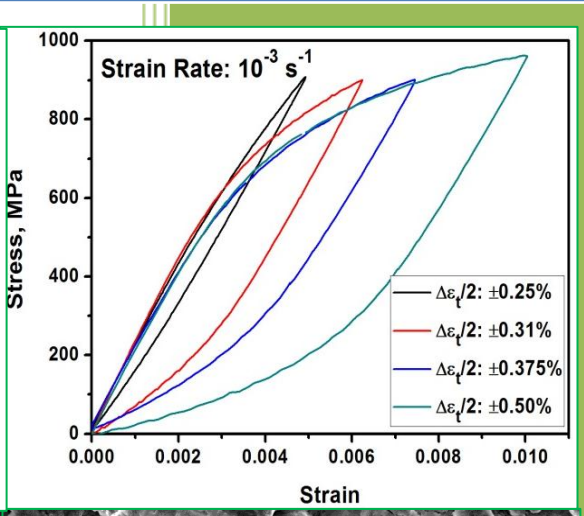

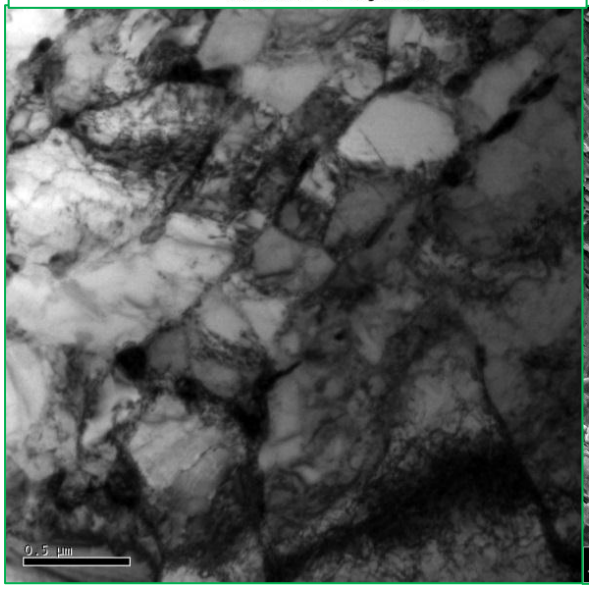

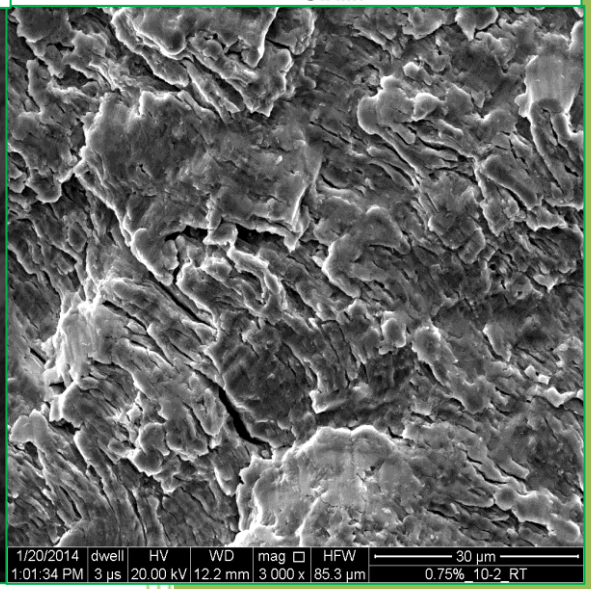

5.1 Introduction

In this chapter low cycle fatigue (LCF) behavior is presented at strain rates from 10^{-2} s^{-1} to 10^{-4} s^{-1} in the regime of low strain amplitude between ±0.25% and ±0.50% at room temperature. The cyclic stress response shows initial mild hardening followed by continuous cyclic softening at all the strain rates. Masing and non–Masing behavior is exhibited at the higher strain amplitudes (≥ ±0.375%) and lower strain amplitudes (< ±0.375%) respectively. Dependence of fatigue life, based on both plastic strain amplitude as well as plastic strain energy is linear and fatigue life decreased with lowering of strain rate. The tempered lath martensitic structure was transformed into equiaxed cell structure at low strain amplitude and to elongated cell structure at high strain amplitude, under cyclic loading. The size of the cells increased with increase in strain amplitude. Thus, the transition of non–Masing to Masing behavior may be related to change in dislocation arrangement from equiaxed cell to the elongated cells. While the friction stress decreases with number of cycles at all the strain amplitudes, back stress remains nearly constant at the high strain amplitudes and increases at the lowest strain amplitude. The observed cyclic softening is thus mainly due to decrease in the friction stress, formation of low energy dislocation cell structure, and annihilation of dislocations.

5.2 Cyclic Stress Response

The variation of cyclic stress amplitude with number of cycles for the different total strain amplitudes at strain rates of 10^{-2} s^{-1}, 10^{-3} s^{-1} & 10^{-4} s^{-1} is shown in Figs. 5.1 a–c respectively. At the highest strain rate of 10^{-2} s^{-1}, there is cyclic softening after the initial 20–30 cycles at the higher strain amplitudes of ≥ ±0.375%, and after 200–300 cycles at the lower strain amplitudes of ≤ ±0.31%.

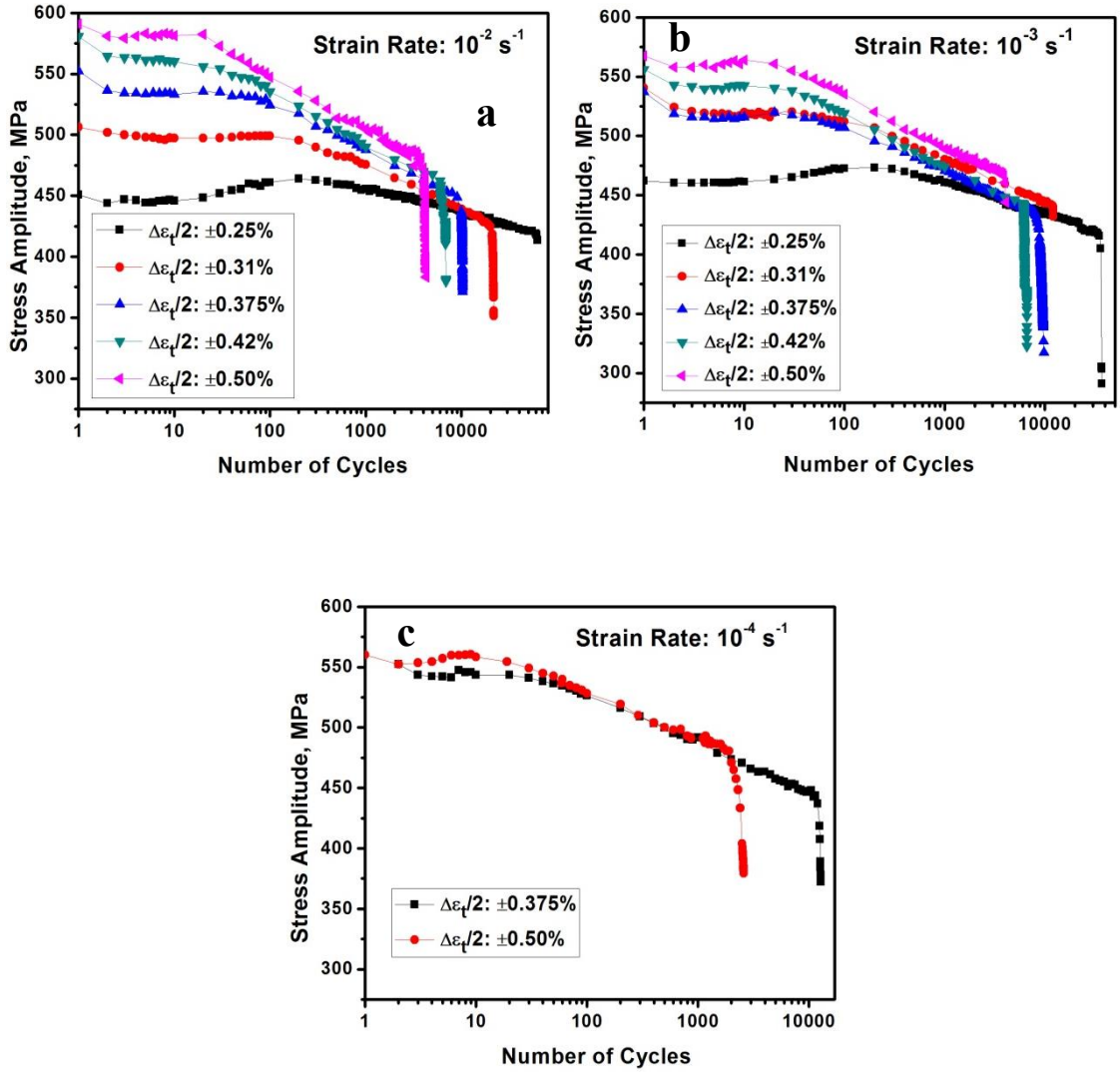

Fig. 5.1 Variation of stress amplitude with number of cycles at different strain rates: (a) 10^{-2} s^{-1}, (b) 10^{-3} s^{-1} & (c) 10^{-4} s^{-1}.

It may be seen that at the highest strain amplitude of ±0.50% there is mild drop in the cyclic stress at the first cycle, followed by mild hardening nearly up to the initial 10–20 cycles. However, at the lowest strain amplitude of ±0.25% after 10 cycles there was marginal cyclic hardening up to about 200–300 cycles, and it is followed by cyclic softening till fracture (Fig. 5.1a). It is noteworthy that the number of cycles to peak hardening increases with decrease in strain amplitude. The degree of cyclic softening increases with increase in strain amplitude. Similar behavior is observed also at the lower strain rate of 10^{-3} s^{-1} (Fig. 5.1b). The differences in the levels of the stress

response curves, at different strain amplitudes are reduced with decrease in strain rate. It may be seen that the stress response curves at the lowest strain rate of 10^{-4} s^{-1}, corresponding to strain amplitudes of ±0.375% and ±0.50%, are almost coincident (Fig. 5.1c).

5.3 Strain–Life Relationship

The strain–based LCF life is widely used to describe the behavior of structural materials operating at elevated temperatures and high levels of stress and strain in power generation plant during their in–service period [130]. In these operations, fatigue damage is generally caused by plastic strain and is described by the Coffin–Manson relationship $\Delta\varepsilon_p/2 = \varepsilon_f'(2N_f)^c$ where ε_f' and c are fatigue ductility coefficient and fatigue ductility exponent respectively [131]. Variation of the number of reversals to failure ($2N_f$) with plastic strain amplitude ($\Delta\varepsilon_p/2$) at different strain rates of 10^{-2} s^{-1} & 10^{-3} s^{-1} is shown in Fig. 5.2 and linear variation of $2N_f$ with $\Delta\varepsilon_p/2$ may be seen on logarithmic scale.

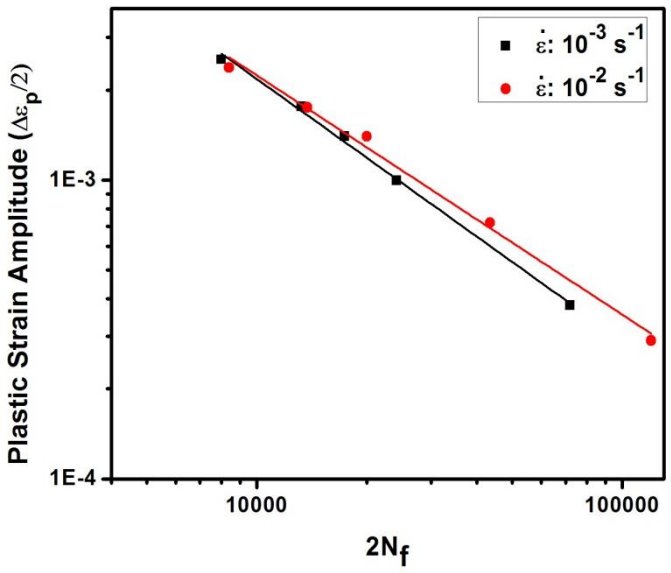

Fig. 5.2 Dependence of fatigue life (as reversals to failure) with plastic strain amplitude, at strain rates of 10^{-2} s^{-1} & 10^{-3} s^{-1}.

The LCF parameters, fatigue ductility exponent (c) and fatigue ductility coefficient (ε_f') are the slope and intercept on Y-axis at $2N_f = 1$ respectively and were determined by least square linear fit of the data in Fig. 5.2. The values of LCF parameters are presented in Table 5.1. Both, fatigue ductility coefficient (ε_f') and fatigue ductility exponent (c) may be seen to increase with decrease in strain rate from 10^{-2} s^{-1} to 10^{-3} s^{-1}. Effect of strain rate on fatigue life at high strain amplitude is found to be negligible, however, fatigue life is lowered at the lowest strain amplitude of ±0.25% at the strain rate of 10^{-3} s^{-1} in comparison with that at the higher strain rate of 10^{-2} s^{-1}.

Table 5.1 LCF parameters at different strain rates based on plastic strain amplitude approach.

Strain Rate (s^{-1})	**Fatigue Ductility Coefficient (ε_f')**	**Fatigue Ductility Exponent (c)**
10^{-2}	3.6442	-0.80434
10^{-3}	6.4835	-0.86978

Cyclic stress strain parameters are calculated from the half–life hysteresis loops at all the strain amplitudes at the different strain rates of 10^{-2} & 10^{-3} s^{-1} and are presented in the Table 5.2. The cyclic strain hardening exponent and cyclic strength coefficient parameters are found to increase with decrease in strain rate (Table 5.2).

Table 5.2 Cyclic stress–strain parameters at different strain rates.

Strain Rate (s^{-1})	**n'**	**K' (MPa)**
10^{-2}	0.03887	675
10^{-3}	0.05333	715

5.4 Strain Energy–Life Relationship

Since LCF damage is associated with cyclic plastic strain, the dissipated strain energy has been considered for accurate prediction of fatigue life of components. In general, fatigue life relationships may be based on stress, strain or energy parameters [132]. The energy parameters have several advantages such as: (a) both strain and stress parameters are included in these models, (b) these variables are independent of the direction by its scalar value, (c) the damage is easy to cumulate, and (d) more suitable to transfer the model results to the real structure.

The plastic strain energy per cycle is equal to the area of the hysteresis loop. In general, the area of the hysteresis loop at half–life is considered as the average plastic strain energy per cycle (ΔW_p). The LCF data were analyzed in terms of power law relationship based on energy [133], similar to the Coffin–Manson relationship.

$$\Delta W_p = W_f'(2N_f)^{\beta}$$

Where W_f' and β are material constants and β is related to the fatigue life constant as $\beta = b + c$. The plot of ΔW_p versus $2N_f$ is shown in Fig. 5.3 and the LCF parameters are presented in Table 5.3. In this approach both W_f' & β are found to decrease with increase in strain rate. Similar dependency of LCF parameters on strain rate is observed in both plastic strain amplitude and energy based approach.

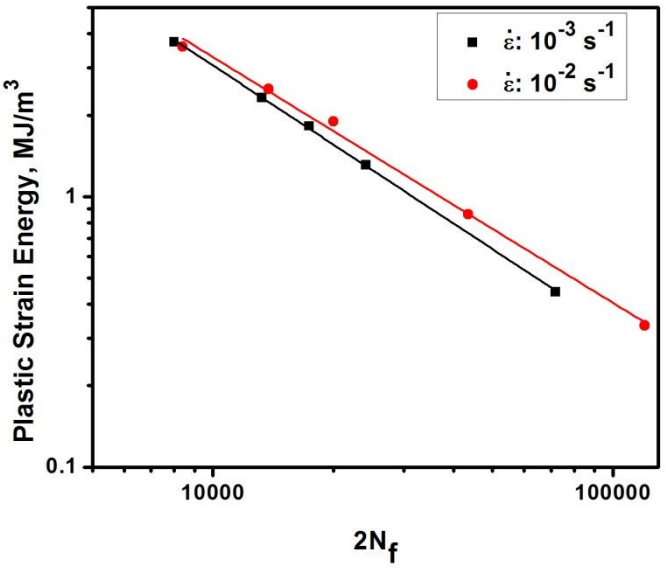

Fig. 5.3 LCF plots based on plastic strain energy and reversals to failure ($2N_f$) at strain rates of 10^{-2} s^{-1} & 10^{-3} s^{-1}.

Table 5.3 LCF parameters at different strain rates, based on plastic strain energy

Strain Rate (s^{-1})	**Fatigue Ductility Coefficient** (W_f')	**Fatigue Ductility Exponent** (β)
10^{-2}	4.12987	-0.90446
10^{-3}	4.37303	-0.9719

5.5 Masing and Non–Masing Behavior

Exhibition of Masing/non–Masing behavior during strain controlled cycling is characteristic feature of a material under LCF. The stress–strain hysteresis loops are analyzed for Masing and non–Masing behavior [134]. A material is said to exhibit Masing behavior if all the translated hysteresis loops follow a similar loading path. On the other hand a material is said to exhibit non–Masing behavior when the stable hysteresis loops do not follow the common loading curve [135,136].

The modified 9Cr–1Mo steel is found to exhibit both Masing and non–Masing behavior depending on the applied strain amplitude in LCF test. Figure 5.4 shows the stress–strain hysteresis loops translated to a common point of maximum compressive stress of saturated hysteresis loop from the different strain amplitudes at strain rates of 10^{-2} s^{-1}, 10^{-3} s^{-1} & 10^{-4} s^{-1}.

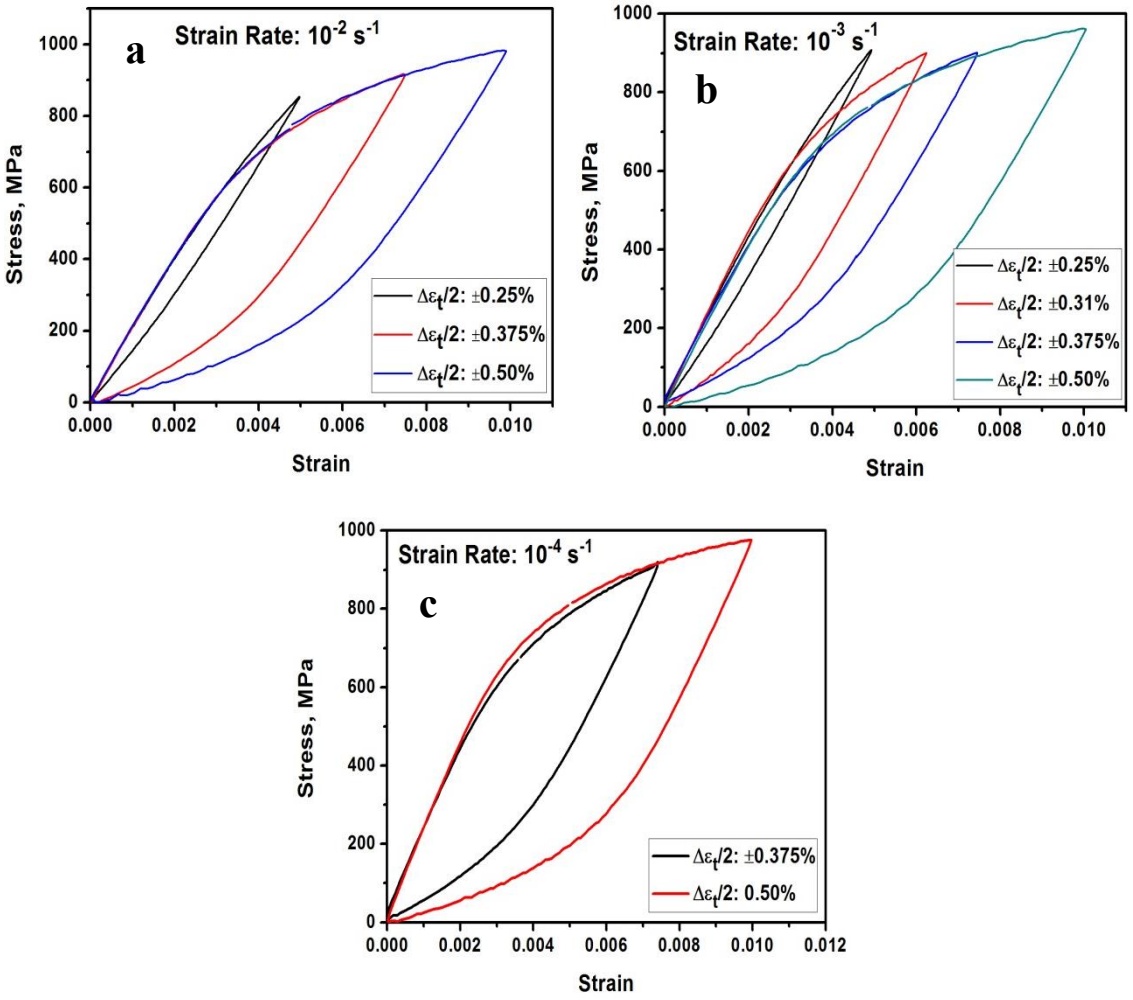

Fig. 5.4 Stress–strain hysteresis loops translated to a common point of maximum compressive stress exhibiting Masing and non–Masing behavior at three different strain rates: (a) 10^{-2} s^{-1}, (b) 10^{-3} s^{-1} and (c) 10^{-4} s^{-1}.

It is obvious that at the strain amplitudes of ≥ ±0.375% the hysteresis loops matches with the tensile portion of the highest strain amplitude whereas the hysteresis

loops of lowest strain amplitude of ±0.25% do not match. Thus, this steel exhibits non–Masing behavior at very low strain amplitude of ±0.25% and Masing behavior at high strain amplitudes ≥ ±0.375%. A quite similar behavior is observed also at the lower strain rates of 10^{-3} s^{-1} & 10^{-4} s^{-1}.

5.6 Dislocation Substructure

The tempered lath martensitic structure (Fig. 3.1c & d) is found to be unstable under cyclic loading and is gradually replaced by subgrain structure. Minimizing their stored energy, the original parallel high dislocation–density martensitic laths partitioned into equiaxed subgrain structure of large size. Figure 5.5 shows dislocation substructures in the specimen tested at different strain amplitudes at strain rates of 10^{-2} s^{-1}. A subgrain structure with relatively low density of dislocations inside the laths and with less/poor defined cell boundary may be seen in the specimen tested at the lowest strain amplitude of ±0.25% (Figs. 5.5 a & b). Elongated cell wall structure with high density of dislocations along cell walls may be seen in the specimen tested at the higher strain amplitude of ±0.375% (Fig. 5.5c). There is intersection of dislocations inside the laths (Fig. 5.5d). Similarly at the highest strain amplitude of ±0.50% there is formation of elongated cell wall structure in some grains and formation of distinct subgrains (Figs. 5.5 e & f).

There is formation of distinct dislocation cell/subgrain structure also at the lowest strain rate of 10^{-4} s^{-1} (Fig. 5.6) and dislocation density inside the grains is high (Fig. 5.6b). However, no elongated cell wall structure was observed at the lowest strain rate of 10^{-4} s^{-1}. It is obvious from Fig. 5.7 that cell size increased with increase in strain amplitude.

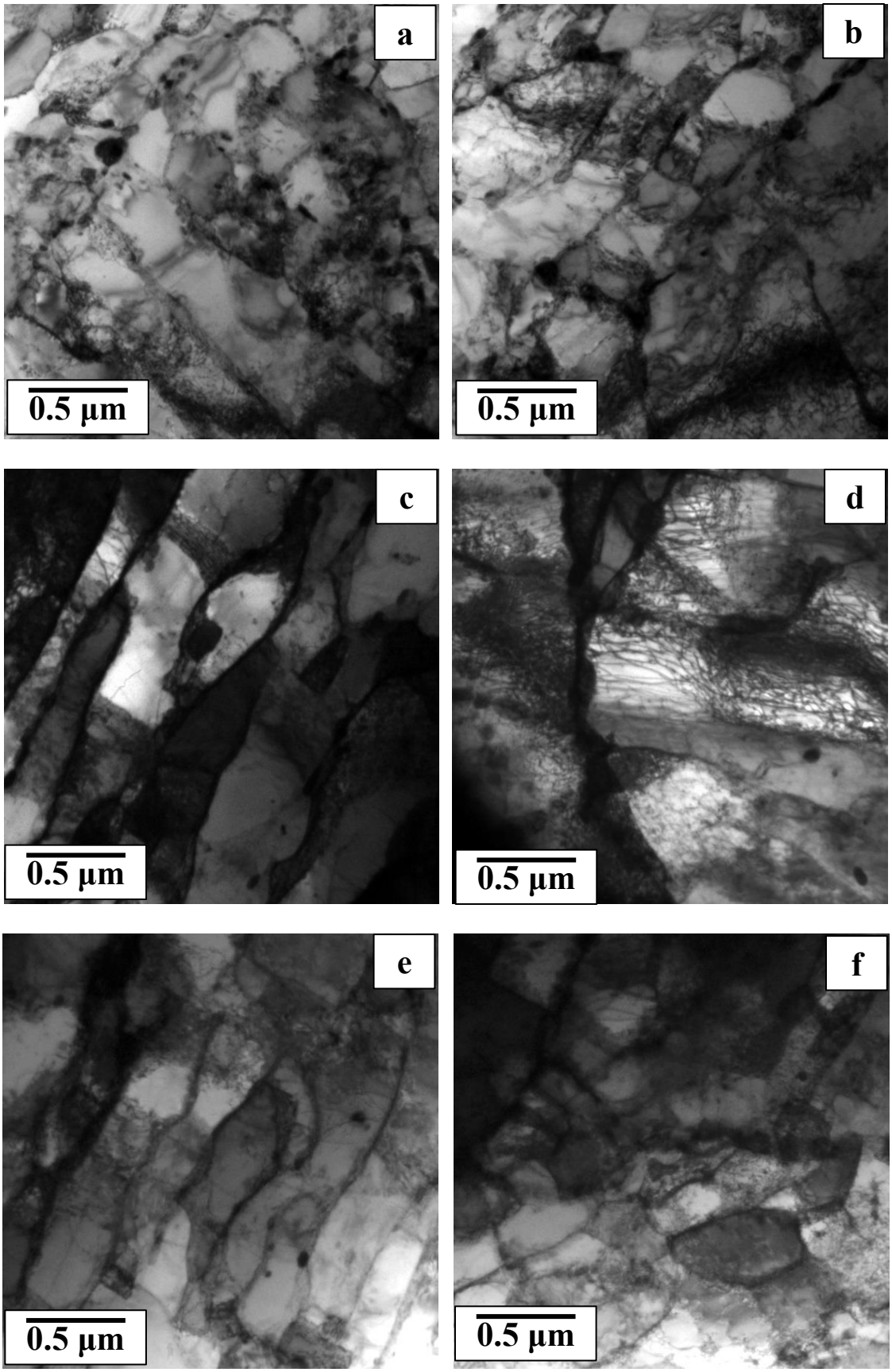

Fig. 5.5 Dislocation configurations resulting from LCF at strain rate of 10^{-2} s^{-1} at different strain amplitudes: (a, b) ±0.25%, (c, d) ±0.375%, (e, f) ±0.50%. Formation of cell structure may be seen at all the strain amplitudes.

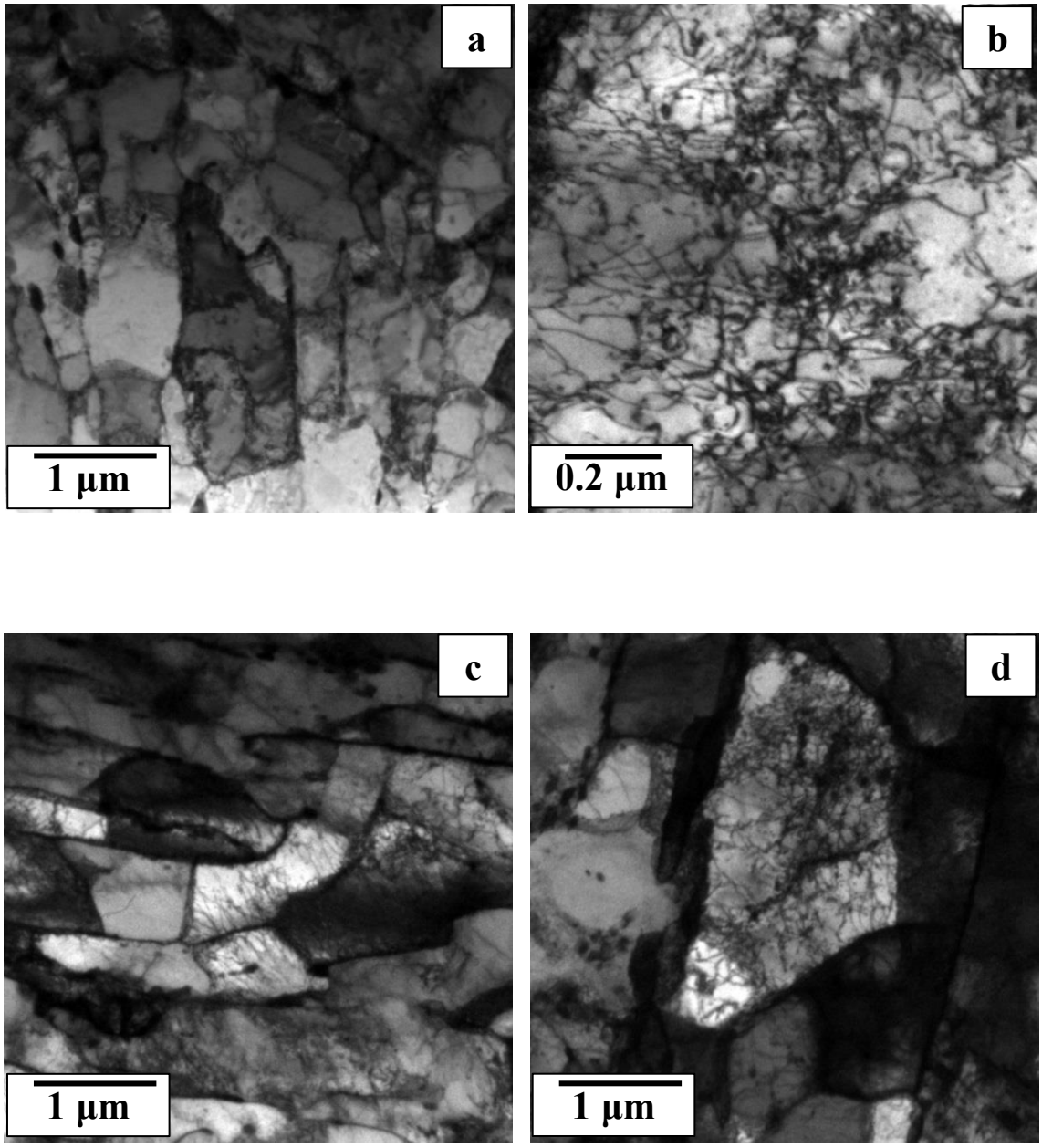

Fig. 5.6 Dislocation configurations resulting from LCF at different strain amplitudes at the lowest strain rate of 10^{-4} s^{-1}:(a, b) ±0.375%; (c, d) ±0.50%.

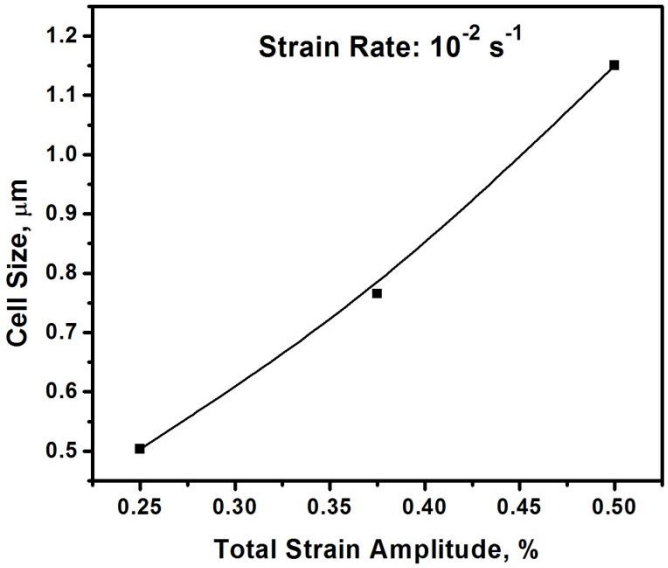

Fig. 5.7 Variation of cell size with strain amplitude, in fatigue tested specimens at strain rate of 10^{-2} s^{-1}.

5.7 Fracture Behavior

Fracture morphology of the fatigue specimens tested at 10^{-2} s^{-1} is shown in Fig. 5.8. It is obvious that there is initiation of multiple cracks with decrease in strain amplitude whereas a sufficiently large single crack form at the highest strain amplitude of ±0.50%. Inter striation spacing is found to increase with increase in strain amplitude. Distinct fatigue striations may be seen from stage II fatigue crack propagation, however, more facets are seen from the right side of the fractographs in Fig. 5.8 A–C. Secondary cracking is observed at higher magnifications at all the strain amplitudes.

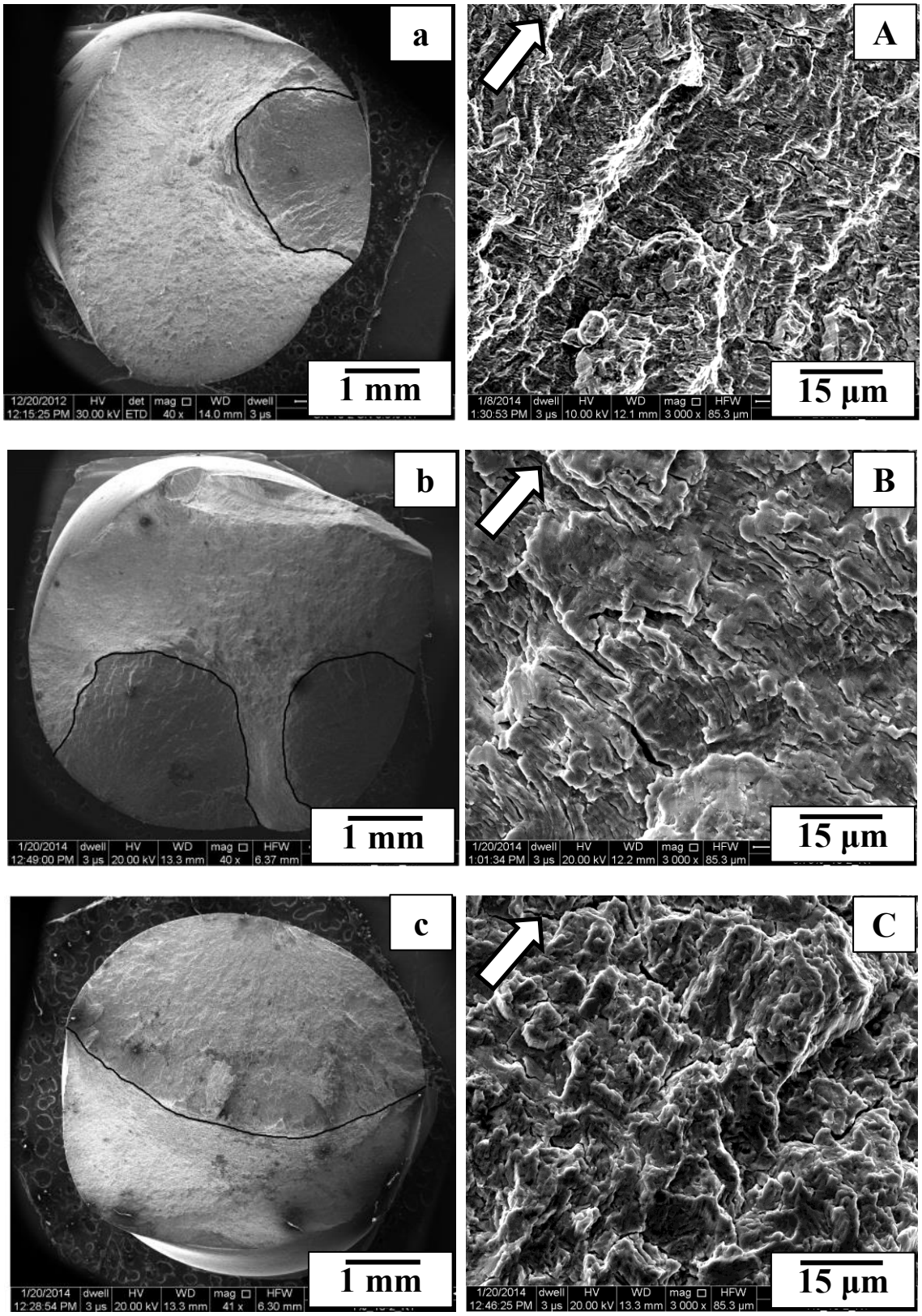

Fig. 5.8 Fracture surfaces of fatigue specimens tested at RT, at strain rate of 10^{-2} s^{-1} at different strain amplitudes: (a, A) ±0.25% (b, B) ±0.375% & (c, C) ±0.50%. The regions of fatigue fracture from surface towards interior are marked by black ink. Striations and secondary cracking are shown in the higher magnification images. Crack propagation direction is shown by white arrows.

Similar fracture morphology is observed even at the lower strain rate of 10^{-3} s^{-1} with multiple crack initiation sites at low strain amplitudes (Fig. 5.9). With increase in strain amplitude to ±0.50%, ratchets are seen as shown by white arrows in Fig. 5.9c.

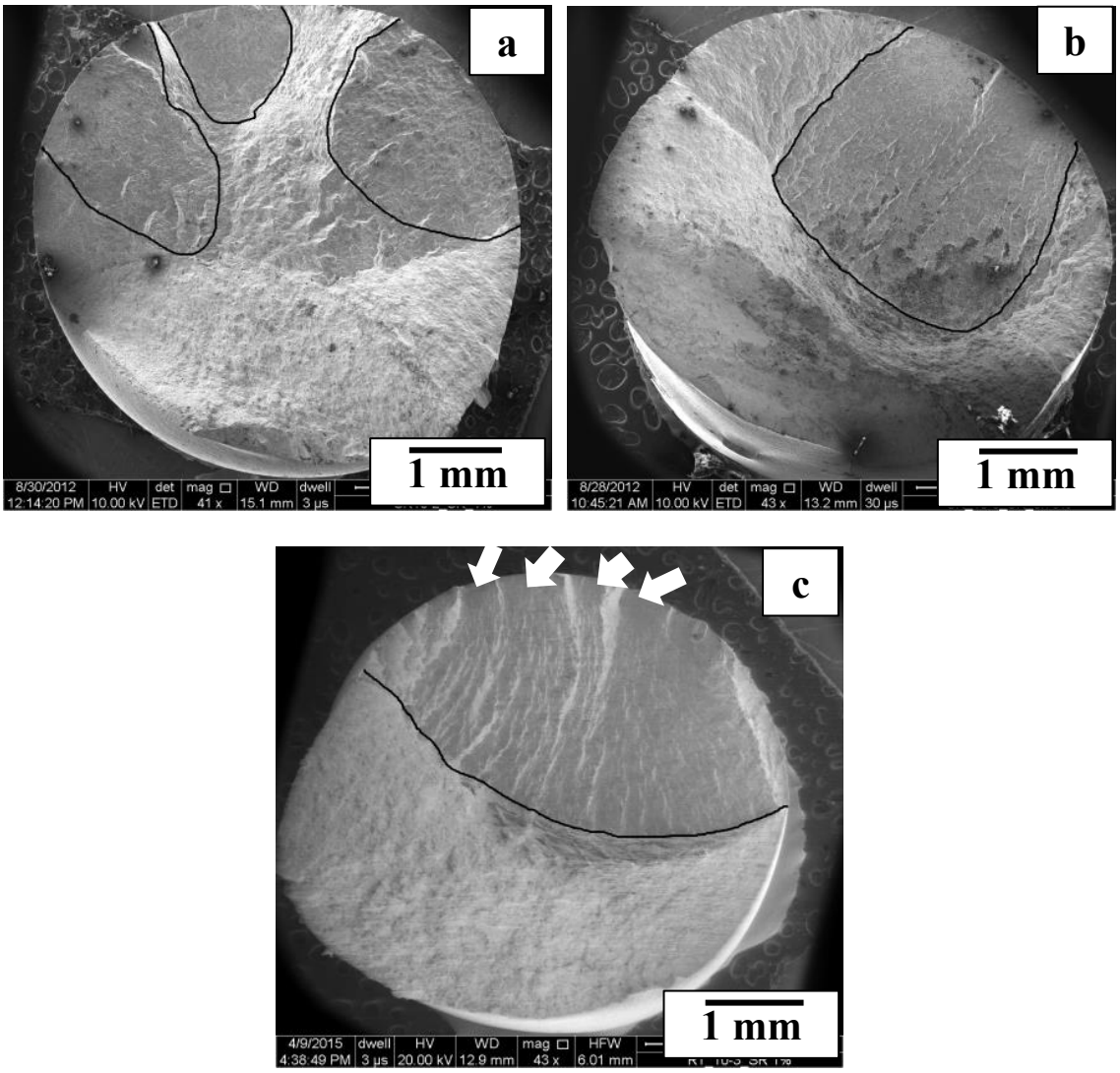

Fig. 5.9 Low magnification fractographs of the LCF tested specimens at strain rate of 10^{-3} s^{-1} at different strain amplitudes: (a) ±0.25%, (b) ±0.375%, (c) ±0.50%. Fatigue regions are marked by black ink and ratchet lines are shown by white arrows.

Ratchet lines are the lines which represent the junction surfaces between the adjacent crack origins. Different microcracks are unlikely to form on the same plane of different heights and their eventual linkage creates a vertical step on the fracture

surface. Once the initial cracks link together, the ratchet lines disappear and follow the same crack propagation path. These lines are shown by arrows in Fig. 5.9c.

Magnified view of the crack initiation site showed that in case of high strain amplitudes, striations are observed just after ~ 50 μm depth from the surface and no striations are visible even up to the depth of ~ 600 μm at low strain amplitude (Fig. 5.10). Tire marks and distinct faceted features are observed in the specimen tested at the lowest strain amplitude of ±0.25% at the strain rate 10^{-3} s^{-1} (Fig. 5.11). Tire marks are characteristic feature of fracture under LCF and result from fatigue crack propagation encountering hard particles such as precipitates, under the reciprocal action of cyclic loading. The crack jumps around the hard particle and then moves forward, leaving an indentation of parallel rows [137]

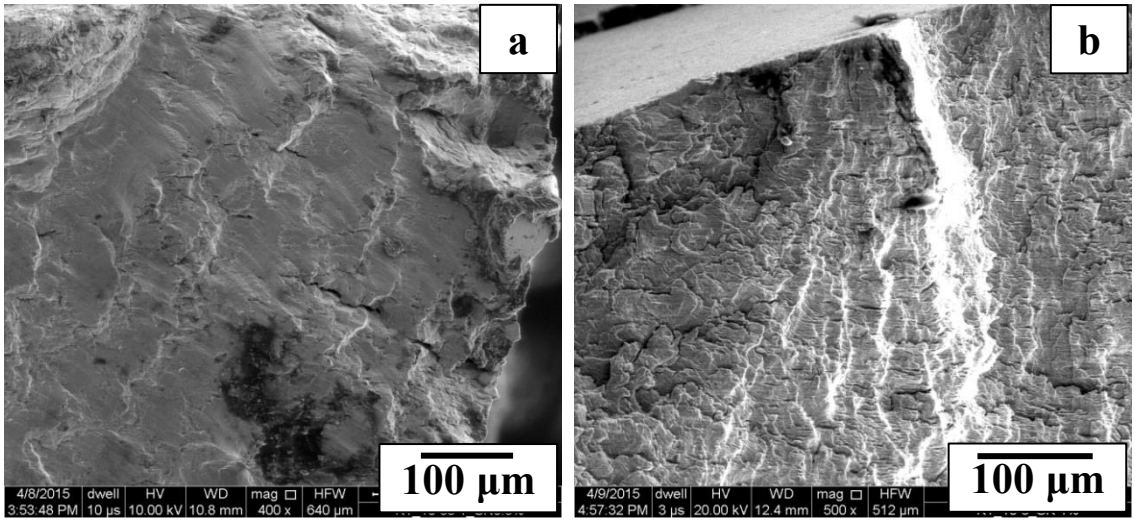

Fig. 5.10 Crack initiation regions resulting from LCF at strain rate of 10^{-3} s^{-1} at different strain amplitudes: (a) ±0.25%, (b) ±0.50%.

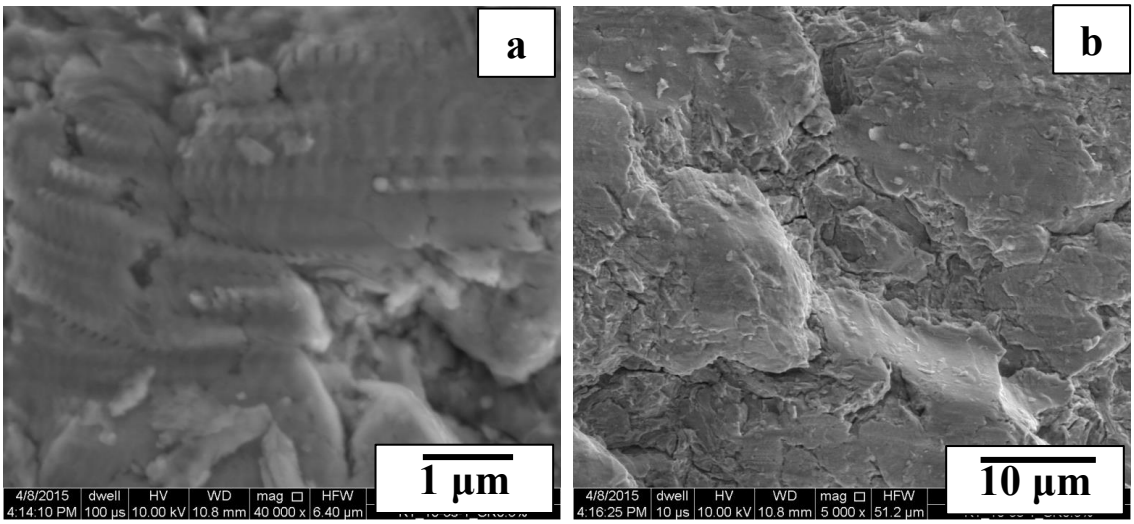

Fig. 5.11 Fractographic images of LCF specimen tested at ±0.25% at strain rate of 10^{-3} s^{-1} showing: (a) tire marks, (b) faceted features.

The areas of both fatigue as well as tensile overload failure were calculated corresponding to both the strain rates and it is found that the area of fatigue region increased with increase in strain amplitude (Table 5.4). Fatigue fracture zone is marked by black solid lines in the fractographs shown in Figs. 5.8 & 5.9.

Table 5.4 Area of the region of fatigue crack propagation at different strain rates of 10^{-2} s^{-1} & 10^{-3} s^{-1}.

Strain Rate (s^{-1})	**Strain Amplitude (%)**	**Area of Fatigue Crack Propagation (%)**
10^{-2}	±0.25	21
	±0.375	24
	±0.50	57
10^{-3}	±0.25	37
	±0.375	40
	±0.50	47

5.8 Discussion

5.8.1 Cyclic Stress Response and Dislocation Substructure

It is obvious from the cyclic stress response curves of the modified 9Cr–1Mo steel that there is initial softening followed by stability up to ~10–20 cycles, mild hardening to peak and finally cyclic softening till fracture (Fig. 5.1). The initial softening is essentially due to movement of free dislocations inside the laths and the subsequent hardening resulted from interaction between the precipitates (MX, X=C/N) and dislocations (Fig. 5.12). $M_{23}C_6$ precipitates were observed mainly at lath boundaries and prior austenite grain boundaries and had pinning influence. This steel in the normalized and tempered condition, with tempered martensite lath structure, is highly unstable under cyclic straining. The laths are gradually replaced by dislocation structure minimizing their stored energy.

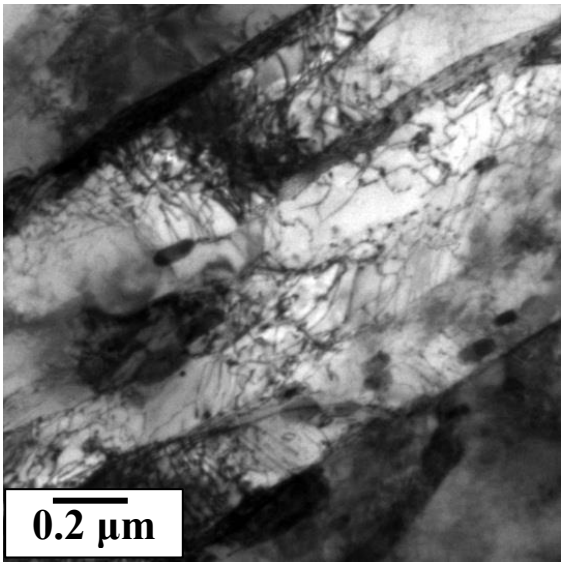

Fig. 5.12 TEM micrograph showing interaction between precipitates (MX) and dislocations in the specimen tested in LCF at strain rate of 10^{-3} s^{-1} and strain amplitude of ±0.25%.

The relatively large extent of cyclic softening at all the strain amplitudes may be attributed mainly to formation of dislocation cell structure, in agreement with earlier observations [65,77,82]. In consequence to early onset of cyclic softening, at high strain amplitudes, there is transformation of lath martensite to subgrain structure, in the early stage.

The dislocation structure is highly heterogeneous with packets of dislocation debris and ill–defined cells in it. The precipitates located along the lath boundaries imposed a pinning effect, resulting in slightly elongated cell structure. Equiaxed dislocation cells are also present. Very fine microalloyed precipitates are found to interact with dislocations in dislocation–rich regions and retard the dislocation motion. It is known that dislocations rearrange themselves during cyclic loading, into a lower energy configuration comprising of dislocation cells, surrounded by dislocation walls, by cross–slip [65,69,80,82].

Size of the subgrains depends on the applied plastic–strain amplitude. It is obvious from Fig. 5.7 that cell size increases with increase in strain amplitude. Dislocation–free areas were frequently observed in the regions close to the lath boundaries at high strain amplitudes. It has been reported that softening stage in 9–12%Cr steels and especially in Reduced Activation Ferritic Martensitic (RAFM) steels is clearly associated with increase in the subgrain size, regardless of the temperature [138] and softening has partially been explained from annihilation of dislocations within subgrains [139] and by lath/sub–grain boundary elimination [140].

As such there is no literature on the effect of strain amplitude and strain rate on deformation behavior and dislocation substructure of the modified 9Cr–1Mo steel, at RT. This steel deforms by more than one slip system. Wavy slip materials are known to attain a stable stress state and a characteristic dislocation substructure, irrespective of

their initial state (hard or soft). In general, cell structure formation is observed in wavy slip materials. On the other hand planar slip materials display different cyclic stabilized stress levels depending on their initial condition and likewise different dislocation substructure. Thus, the development of a characteristic dislocation substructure i.e. cell structure in the cyclically deformed modified 9Cr–1Mo steel, a wavy slip material, is there in all the test conditions, irrespective of strain amplitude and strain rate. It may be stated that there is no change in the dislocation configuration due to change in the test condition.

5.8.2 Role of Friction and Back Stress

Friction stress and back stress are well established key parameters to describe dislocation movement under constant strain control fatigue [136]. The friction stress arises from the resistance to dislocation movement in the lattice involving short–range interaction obstacles and back stress results from long–range interaction obstacles [141,142]. In the present investigation, the friction stress and back stress are determined to find out their contribution in cyclic stress response of the tempered martensitic steel. These parameters are calculated from the stress–strain hysteresis loops for all the cycles, at all the strain amplitudes, as per the procedure proposed by Cottrell's scheme [143] and employed by Kuhlmann–Wilsdorf and Laird [144].

At the start of plastic deformation in the direction of tensile loading of a strain cycle a back stress (σ_b^t) had been generated in the preceding cycle, then in the presence of friction stress (σ_f^t) the yield strength (σ_y^t) can be expressed as

$$\sigma_y^t = \sigma_f^t - \sigma_b^t \quad \text{..... (I)}$$

At the end of strain cycle in the tensile direction when the back stress reached its maximum value the stress was equal to

$$\sigma_{max}^t = \sigma_f^t + \sigma_b^t \quad \text{..... (II)}$$

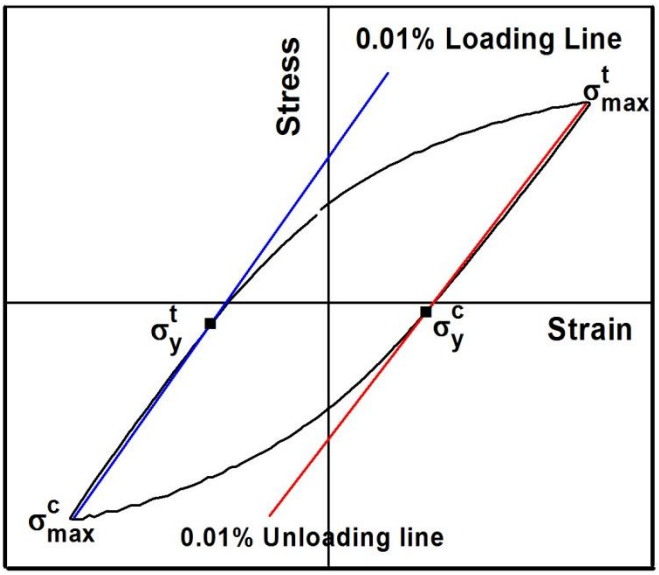

Fig.5.13 Schematic of the hysteresis loop illustrating the different components of stress for calculation of friction and back stress.

From equation (I) and (II)

$$\sigma_f^t = (\sigma_{max}^t + \sigma_y^t)/2 \quad \text{..... (III)}$$

$$\sigma_b^t = (\sigma_{max}^t - \sigma_y^t)/2 \quad \text{..... (IV)}$$

Similarly, the friction stress and back stress in the compression direction would be as follows.

$$\sigma_f^c = (\sigma_{max}^c + \sigma_y^c)/2 \quad \text{..... (V)}$$

$$\sigma_b^c = (\sigma_{max}^c - \sigma_y^c)/2 \quad \text{..... (VI)}$$

The yield stress in tensile (σ_y^t) and compressive (σ_y^c) direction was taken as offset stress at a deviation of 0.01% from the linear portion of the hysteresis loop as shown in Fig. 5.13.

Figure 5.14–5.16 shows variation of friction stress and back stress with number of cycles at the different strain amplitudes corresponding to strain rates of 10^{-2}, 10^{-3} & 10^{-4} s^{-1} respectively. It is obvious that friction stress decreases with number of cycles at

all the strain amplitudes, at all the strain rates, whereas the back stress is nearly constant at the higher strain amplitudes and increases at the lowest strain amplitude.

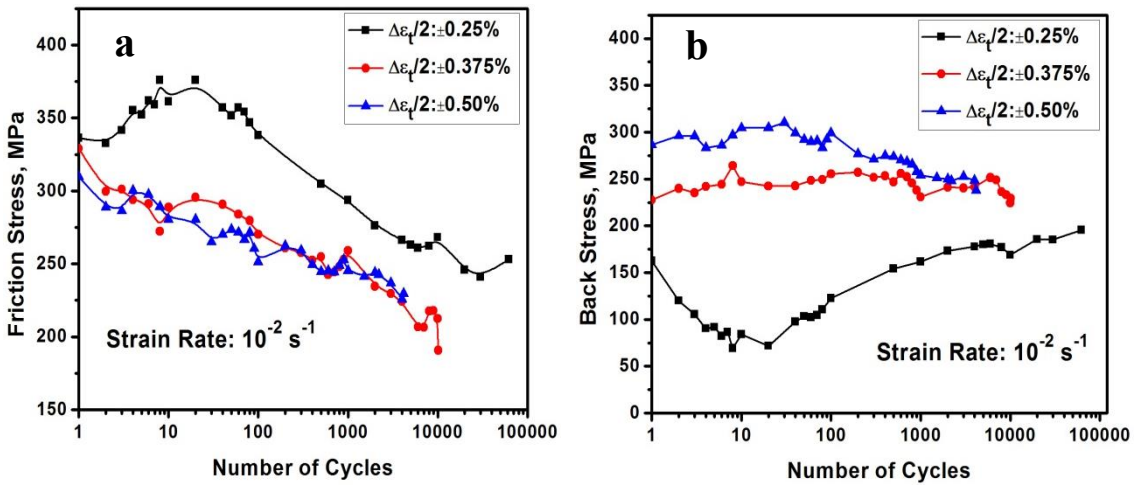

Fig. 5.14 Variation of friction and back stress with number of cycles at different strain amplitudes at strain rate of 10^{-2} s^{-1}: (a) friction stress, (b) back stress.

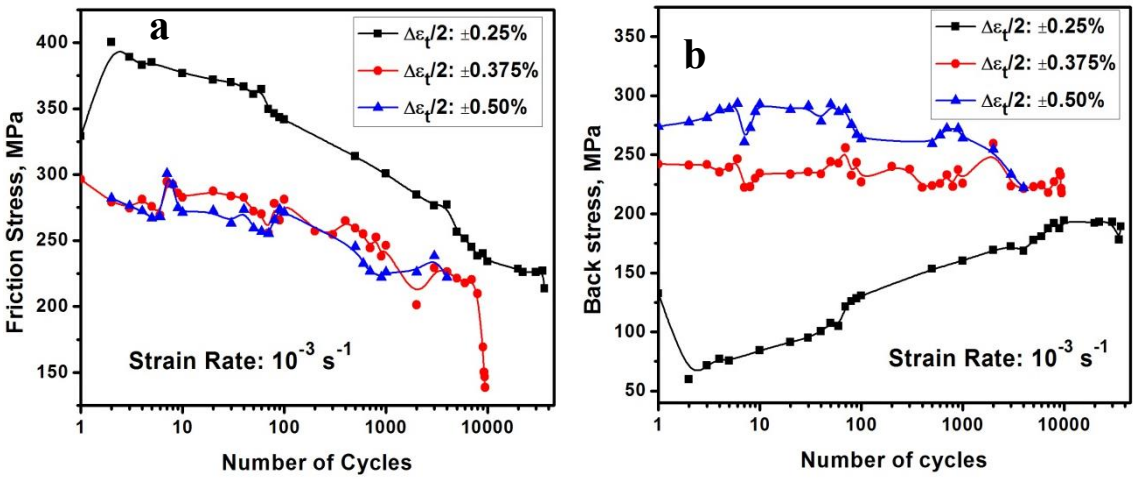

Fig. 5.15 Variation of friction and back stress with number of cycles at different strain amplitudes at strain rate of 10^{-3} s^{-1}: (a) friction stress, (b) back stress.

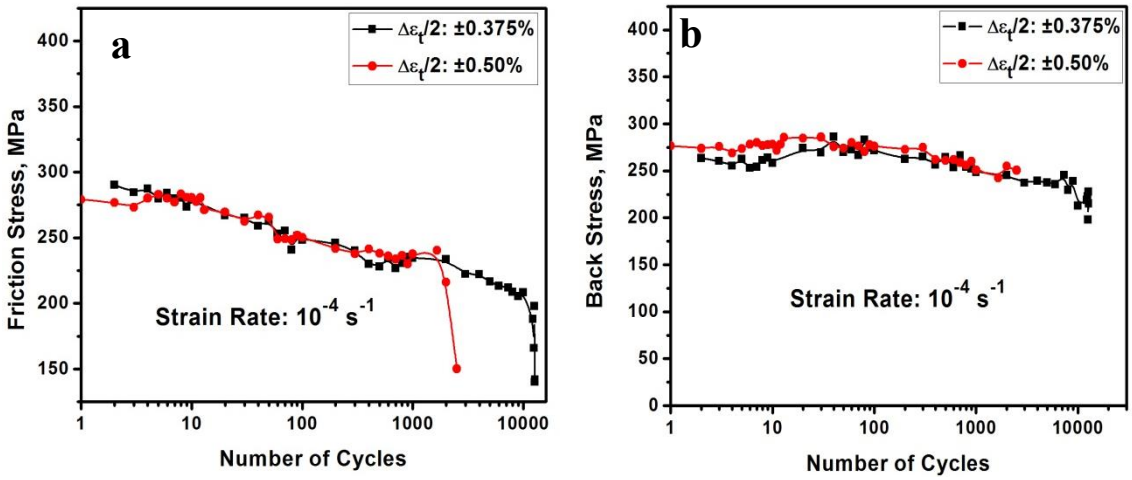

Fig. 5.16 Variation of friction and back stress with number of cycles at different strain amplitudes at strain rate of 10^{-4} s^{-1}: (a) friction stress, (b) back stress.

Fournier et al. [68] studied microstructural evolution and cyclic softening of this steel at 550 °C at different strain amplitudes from ±0.20% to ±0.50%. The softening of the steel is directly correlated to decrease in the kinematic stress (back stress) which arises from 'directional and long–range' obstacles to movement of dislocations. Therefore, grain and subgrain boundaries (through a dislocation pile–up mechanism) and, more generally, all microstructural heterogeneities (arrangement of dislocations, precipitates, etc.) are sources of kinematic hardening. This suggests that, during cycling the softening occurs from disappearance of microstructural heterogeneities [69]. Krishna et al. [78] have analyzed the effect of the temperature on cyclic stress response at RT, 550 and 600 °C at high strain amplitudes (± 0.70% to ±1.2%), at strain rate of 10^{-3} s^{-1}. They observed that decrease in the effective stress (friction stress) had a dominating effect over the decrease in internal stress (back stress) and the cyclic yield stress decreased with increase in test temperature, however both the stresses decreased with increase in test temperature [78].

Based on the results of the present investigation it is important to mention that at all the strain amplitudes the cyclic stress response is controlled primarily by friction stress.

5.8.3 Analysis of Masing and Non–Masing Behavior

Effect of cyclic strain amplitude was analyzed on Masing/non–Masing behavior of this steel in the normalized & tempered condition. There is Masing behavior at high strain amplitudes (≥ 0.375%) and non–Masing at low strain amplitudes (< ±0.375%) as shown in Fig. 5.4. Usually, the change from Masing to non–Masing behavior is associated with transformation of dislocation substructures to dislocation cell structures [145]. Thus, in the present investigation transition from non–Masing to Masing behavior may be understood in terms of change in the equiaxed cell structure at low strain amplitude to elongated cell structure at high strain amplitudes. Masing and non Masing behavior in the modified 9Cr–1Mo steel has earlier been studied by Krishna et al. [78] at RT. They found Masing behavior at strain amplitudes from ±0.70% to ±1.0% and non–Masing behavior at strain amplitude from ±1.1% to ±1.2% at RT. Plumree et al. [145] observed Masing behavior for metals with finely dispersed particles and single phase low stacking fault metals; and non–Masing behavior in high stacking fault energy materials, in which the deformation was mainly controlled by the matrix. Depending on the strain amplitude, ferritic–pearlitic AISI 1018 hot rolled steel was found to exhibit Masing behavior at low strain amplitudes and non–Masing at higher strain amplitudes. It is important to mention that all the previous investigations have been conducted at higher strain amplitudes (> ±0.50%) where Masing behavior was observed. The occurrence of Masing behavior at strain amplitudes ≥ ±0.375% in the present investigation is in line with the earlier investigation [78]. However, it is

noteworthy from the present investigation that there was non–Masing behavior at the very low strain amplitude of ±0.25%. Thus, there was transition from the Masing to non–Masing behavior from high to low strain amplitude.

5.8.4. Fracture Behavior

The largest portion of fatigue fracture consists of Stage II crack growth exhibiting striations on fracture surface, and is more influenced by strain amplitude and microstructure [146–148]. In general, a large portion of fatigue life is spent in crack nucleation in stage I at low strain amplitudes and stage II crack growth at high strain amplitudes. Thus, the decrease in fracture area corresponding to stage I with increase in strain amplitude from ±0.25% to ±0.50% and increase in the stage II area with increase in strain amplitude may be understood (Fig. 5.10). The microstructure and mechanical properties of the materials strongly affect the process of crack initiation and its subsequent propagation. In the ferritic–martensitic steel (EUROFER 97) lath boundaries are favorable sites for microcrack nucleation [149]. Slip irreversibility occurs in materials and plastic strain accumulates during fatigue loading. At the defect level, the irreversibility is a result of dislocation pile–up, annihilation or cross–slip. Grain boundary or inclusion–matrix phase boundary also contribute to slip irreversibility. These slip irreversibilities are considered early signs of damage during cyclic loading.

The dislocations subsequently form low–energy stable structures as means to accommodate the irreversible slip processes and modify the dislocation density during forward and reverse cyclic loading. Inclusions and precipitates are special defects that can initiate cracks because of different factors such as slip characteristic of the matrix, the relative strength of the matrix and inclusions, strength of the matrix inclusion interface and environmental factors. Depending upon the structure relationship between the matrix and precipitates, these interfaces could be weakest sites of a material. Matrix

and precipitates may raise the mechanical stress in vicinity of the interface during cyclic loading causing, eventual interfacial crack initiation.

Also faceted features are observed in the region of stage II crack growth without striation markings, prominently more at the high strain amplitudes, at the strain rate of 10^{-2} s^{-1} and even at low strain amplitudes at lower strain rate of 10^{-3} s^{-1} (Fig. 5.8, 5.11). The occurrence of tire marks and faceted fracture with decrease in strain amplitude and strain rate may clearly be seen from Fig. 5.11.

In the early stage of cracking arising from cyclic straining there were faceted features and ΔK would have been very low. As the fatigue crack started propagating distinct striation marks were visible. It may be noted that the fatigue crack propagating can occur even without formation of striations at high and low ΔK values, irrespective of the type of material [150]. Striations formed at intermediate ΔK because at high ΔK plastic blunting mechanism operates causing microvoid coalescence while at low ΔK values crystallographic orientation dependence leads to formation of cleavage like facets. Ratchet marks are another macroscopic feature that can be observed in fatigue fracture. These marks originate when multiple cracks are nucleated at different points/heights in gage section of the specimen. Since each microcrack is unlikely to form on the same plane eventual linkage of such cracks leads to formation of vertical step on the fracture surface. Once the initial cracks link together, the ratchet lines disappear. Therefore, the number of ratchet marks is a good indication of the number of nucleation sites. As the applied stress increases, the number of nucleation sites and associated ratchet lines increases [150]. It is obvious that crack initiation sites increased with decrease in strain rate and ratchet line formation was more prominent at the high strain amplitude of ±0.50% at low strain rate (Fig. 5.9c). Thus, the decrease in fatigue life with decrease in strain may be due to increase in the crack initiation (ratchet line)

sites. Area of the fatigue fracture zone is found to increase with increase in strain amplitude. Smaller area of fatigue failure at the lowest strain amplitude of ±0.25% may be understood from the fine inter striation spacing as compared to that at high strain amplitude. It may be stated that more number of cycles can be accommodated in less area due to fine inter striation spacing.

5.9 Conclusions

The following conclusions may be drawn from this chapter:

- In general, the modified 9Cr–1Mo steel exhibits cyclic softening at all the strain amplitudes and the strain rates investigated. There is drop in stress in the very first cycle and mild hardening during the subsequent cycles up to 20–30 cycles at the higher strain amplitudes (≥ ±0.375%) and up to 200–300 cycles at the lowest strain amplitude of ±0.25%.
- Fatigue life based on both plastic strain amplitude as well as plastic strain energy increases linearly with decrease in these parameters.
- Irrespective of strain amplitude and strain rate there was transformation of unstable martensite lath structure to dislocation sub–grain structure under cyclic loading by forming dislocation cell structure. The cell size increased and density of dislocations increased with increase in strain amplitude. The cyclic softening in the steel may thus be attributed to formation of lower energy dislocation cell structure.
- Both at high as well as low strain amplitude softening is controlled essentially by the friction stress which continuously decreased with number of cycles.
- The stable hysteresis loops displayed Masing behavior at higher strain amplitudes (≥ ±0.375%) and non Masing behavior at lower strain amplitudes

(< ±0.375%) and this may be due to change in equiaxed cell structure to elongated cell structure.

- There is fall in fatigue life with decrease in strain rate, which may be correlated with the more faceted nature of fracture and more crack initiation sites.